

Earlier peak photosynthesis timing accelerates wildfire outbreak and expands burned area

Chaoyang Wu (✉ wucy@igsnrr.ac.cn)

Institute of Geographic Sciences and Natural Resources Research <https://orcid.org/0000-0001-6163-8209>

Genke Lai

Nanjing University

Jialing Li

Nanjing University

Jun Wang

Chinese Academy Sciences

Yongguang Zhang

Nanjing University <https://orcid.org/0000-0001-8286-300X>

Constantin Zohner

ETH Zurich <https://orcid.org/0000-0002-8302-4854>

Josep Penuelas

CSIC, Global Ecology Unit CREAF-CSIC-UAB, Cerdanyola del Vallès 08193, Catalonia, Spain

<https://orcid.org/0000-0002-7215-0150>

Biological Sciences - Article

Keywords:

Posted Date: August 2nd, 2023

DOI: <https://doi.org/10.21203/rs.3.rs-3189924/v1>

License:   This work is licensed under a Creative Commons Attribution 4.0 International License.

[Read Full License](#)

Abstract

The frequency and intensity of wildfires in recent decades have reached unprecedented levels¹⁻³, raising questions about the role of vegetation phenology in driving these changes. By examining both terrestrial fire perimeters and satellite observations, we found that an earlier peak photosynthesis timing (PPT) contributes to the acceleration of wildfire outbreaks and the expansion of burned areas across the Northern Hemisphere. This correlation can be attributed to intensified drought conditions and an increased leaf supply resulting from earlier senescence. We further show that current fire-vegetation models are capable of reproducing the negative correlation between PPT and burned area, but they significantly underestimate the strength of this relationship. Our findings provide valuable insights for enhancing early wildfire detection and prediction methods by considering the feedback effects of vegetation on fire risk.

Introduction

The intensification of wildfires in recent decades has had significant impacts on the land surface, with far-reaching consequences for global carbon uptake and ecosystem functioning^{4,5}. Both local and regional observations have provided evidence of a notable increase in the frequency and intensity of wildfires^{2,6}. However, understanding the underlying reasons for these changes is a complex task. Climate change, for example, has amplified the risk of extreme wildfires through rising temperatures and declining atmospheric humidity⁷. Additionally, the impact of climate change on wildfires can be influenced by changes in vegetation productivity, either exacerbating or mitigating the risks⁸. Therefore, it is crucial to gain a better understanding of how vegetation feedbacks drive wildfires to improve early warning systems and estimate carbon emissions under future climate change scenarios.

The mid-high latitudes of the Northern Hemisphere play a critical role in wildfire dynamics, as boreal wildfires alone accounted for approximately one-quarter of global fire carbon dioxide emissions in 2021³. Moreover, these regions have undergone substantial climate warming, resulting in substantial changes in vegetation growth^{9,10}. These changes in vegetation dynamics can in turn feedback to climate through biophysical and biogeochemical processes, thereby modulating seasonal cycles of energy and water fluxes and landscape properties¹¹. For example, an earlier onset of growth in spring may exacerbate summer soil drying due to large increases in evaporative water loss¹². This prolonged soil water depletion can cause more severe and longer droughts and heat waves^{12,13}. The advanced leaf-out additionally enhances surface warming through feedbacks on water vapor, snow albedo and solar radiation¹⁴.

To explore the hypothesis that vegetation growth during the summer period contributes to the occurrence and extend of subsequent wildfires, we conducted a comprehensive analysis using various datasets and models. We analyzed long-term series from 2001 to 2018 of terrestrial fire perimeters, satellite-derived burned area (BA) (Supplementary Fig. S1), maximum photosynthesis and its timing from novel satellite solar-induced chlorophyll fluorescence (SIF) and normalized difference vegetation index (NDVI) data

(Supplementary Fig. S2), as well as climate and meteorological variables (Table S1). To investigate the feedback loops between advanced summer phenology and fire-season drought conditions, we employed an earth system model. Furthermore, we examined the relationship between peak vegetation photosynthesis and burned area in state-of-the-art fire-vegetation models participating in the Fire Model Intercomparison Project (FireMIP; Table S2). Integrating these diverse datasets and models allowed us to explore the connections between vegetation phenology, climate conditions, and subsequent fire activity.

Results

Our analysis revealed significant effects of peak photosynthesis timing (PPT) on wildfire timing (FT) and burned area (Fig. 1). SIF-based PPT (PPT_{SIF}) had a strong predictive relationship with both wildfire occurrence and BA. Across the majority of pixels of Northern Hemisphere (65.2%), an earlier PPT_{SIF} led to significant (p -value<0.1) advances in wildfire timing, as determined by terrestrial fire perimeters (FT_{FP}), whereas a delaying effect was only found for 3.4% of pixels (Fig. 1a1). Regarding BA_{FP} , we observed a predominantly negative correlation with PPT_{SIF} , with 42.9% of pixels showing a significant increase in burned area with earlier PPT, whereas the opposite was found for only 2.4% of pixels (Fig. 1a2). Consistent results were obtained with remote sensing wildfire products (Fig. 1a3-a4).

By contrast, the maximum SIF (SIF_{max}) had limited effects on wildfire occurrences, as we observed comparable proportions of significant positive and negative correlations (13.9% vs. 10.0%, Fig. 1b1) with FT_{FP} . Similar patterns were observed for BA_{FP} (Fig. 1b2). The remote sensing wildfire products corroborated these findings, showing no dominant positive or negative relationships between SIF_{max} and FT/BA (Fig. 1b3-b4).

In addition to characterizing vegetation peak growth using SIF, we also characterized it using NDVI. Aligning with the SIF-based analysis, the timing of peak photosynthesis (PPT_{NDVI}) outperformed its amplitude ($NDVI_{max}$) in predicting FT and BA for both the terrestrial fire perimeters (Fig. 1c1-c2, d1-d2) and the remote sensing wildfire products (Fig. 1c3-c4, d3-d4). This demonstrates a high level of consistency between the results obtained from SIF and NDVI data, particularly in terms of the direction of correlations (Extended Data Fig. 1).

Our analyses provided additional insights into the relationship between peak photosynthesis timing and wildfire outbreak and burned area, highlighting the mediating role of multiple factors (Fig. 2). PPT_{SIF} exhibited an overall negative correlation with atmospheric vapor pressure deficit (VPD), with 53.5% of pixels showing significant (p -value<0.1) increases in VPD with earlier PPT. In contrast, only 4.0% of pixels exhibited decreases in VPD with earlier PPT (Fig. 2a). Similar patterns were observed for the climatic water deficit (CWD), with 42.6% of pixels showing significant increases in CWD with earlier PPT, and only 6.5% of pixels showing the opposite effect (Fig. 2b). Furthermore, we identified a positive relationship between PPT_{SIF} and the date of foliar senescence (DFS_{SIF}), with an earlier PPT leading to significantly earlier senescence in 47.5% of the pixels, while only 2.6% of pixels showed the opposite effect (Fig. 2c).

Consistent results were obtained when analyzing NDVI data (Fig. 2d-f). Considering the impacts of VPD, CWD, and DFS on wildfire outbreak and burned area as shown in Extended Data Fig. 2, these variables act as mediators between peak photosynthesis timing and wildfire activity. These findings were also supported by the analysis of terrestrial fire perimeters (Extended Data Fig. 3a-f and 4).

To better understand the individual connections between these variables, we conducted a path analysis, establishing three pathways linking peak photosynthesis timing and wildfire activity: PPT-VPD-wildfire, PPT-CWD-wildfire, and PPT-DFS-wildfire (Supplementary Fig. S3). Consistent with the partial correlation analyses (Fig. 1), the path analysis showed that earlier PPT_{SIF} led to earlier wildfire timing (FT_{MODIS}) and an increase in burned area (BA_{MODIS}) (Fig. 2g-h). The most significant pathway influencing wildfire timing and burned area was the senescence effect ("PPT-DFS-wildfire" path, Fig. 2h). This indicates that an earlier PPT enhances wildfire activity primarily by advancing senescence dates. A likely explanation is that the advancement in senescence stimulates wildfire activity by increasing the accumulation of dry and dead plant material throughout the leaf senescence period (Supplementary Fig. S4). Furthermore, the link between earlier PPT_{SIF} and increased VPD and CWD can likely be explained by biophysical feedback mechanisms, further amplifying wildfire activity (Fig. 2g-h). These potential mechanisms were also supported by additional analyses using NDVI data (Fig. 2i-j) and terrestrial fire perimeters (Extended Data Fig. 3g-j). Overall, these analyses provide strong support that PPT enhances wildfire activity by advancing senescence dates and increasing VPD and CWD.

The observations and modeling results provide insights into the climate feedbacks resulting from advanced summer phenology in northern ecosystems, shedding light on how fire-season drought conditions respond to PPT. We employed the Community Earth System Model 2.2 to provide mechanistic insights into these climate feedbacks (see Methods for details). The simulations showed that a 10-day earlier PPT in temperate and boreal trees led to an enhanced summer-autumn warming in most regions of the Northern Hemisphere (Fig. 3a-b). This warming effect, in turn, influenced precipitation patterns. Specifically, in broad swaths of Eurasia and North America, advanced summertime vegetation activity resulted in reduced rainfall during summer and autumn (Fig. 3c). The combination of warmer air temperature and decreased precipitation contributed to higher VPD and CWD in most temperate and boreal regions (Fig. 3d-e). Additionally, surface soil moisture was reduced due to warmer and drier conditions, particularly in the Pacific United States, Northwest Canada and East Siberia (Fig. 3f). These regions have also experienced remarkable increasing trends in burned area over the past two decades⁸. Therefore, the observations and the earth system model consistently indicate that advanced PPT can exacerbate drought conditions, creating more favorable conditions for wildfires.

The advanced summer phenology has mechanistic impacts on the seasonal patterns of vegetation evapotranspiration, leading to increased vegetation-induced moisture flux in early summer but less in the following months (Extended Data Fig. 5a-c). Consequently, the surface sensible heat from July to September is increased, resulting in higher daily maximum temperatures and enhanced growth of the planetary boundary layer (Extended Data Fig. 5d-f). With reduced surface water vapor input and a deeper planetary boundary layer, there is a more efficient boundary-layer mixing of moisture. This tends to inhibit

the formation of low-level clouds and local convective precipitation (Extended Data Fig. 5g-h). As a result, there is a decrease in cloud coverage and precipitation, leading to greater land-surface sensible heating through increasing downward solar radiation and decreased latent heat flux. This, in turn, brings about a further warming of the surface. The pattern of large-scale precipitation change appears to be noisy, possibly due to vegetation-induced disturbances in the large-scale circulation regimes (Extended Data Fig. 5i). Therefore, the enhanced VPD and CWD due to advanced summer phenology appear to primarily arise from a warmer surface, declined convective precipitation and land-air feedbacks.

To assess the representation of the observed relationship between PPT and wildfire activity in state-of-the-art fire-vegetation models, we used seven models participating in the FireMIP that simulate seasonal variations in vegetation photosynthesis (represented by gross primary productivity, GPP) and wildfire activity (represented by burned area)¹⁵. These models employ empirical and process-based approaches and incorporate the impacts of climate conditions, vegetation productivity, and human activities on fire occurrence^{15,16}. We found that the FireMIP models were able to replicate the correlation between PPT and BA in northern ecosystems, showing a predominantly negative relationship that aligned with the satellite-derived SIF observations (Fig. 4a-h). However, further sensitivity analysis revealed that most FireMIP models could not reproduce the magnitude of this effect. On average, the models underestimated the sensitivity of BA to PPT by 270% when compared with satellite SIF observations (Fig. 4i and Extended Data Fig. 6). Notably, the Community Land Model, which serves as the land model for the Community Earth System Model, performed comparatively better than the other FireMIP models in replicating the observed relationship between PPT and burned area, underestimating the sensitivity by only 28%.

Discussion

In recent decades, the frequency and intensity of wildfires have reached unprecedented levels, due to changes in various factors, including fuel availability, aridity, ignition sources, and extreme fire weather conditions that promote fire spread¹⁷. While previous studies have primarily focused on the impacts of climate change on annual-scale wildfire activities⁷, the influence of vegetation growth and phenology on wildfires has received less attention. However, vegetation growth and phenology can provide feedback to the climate system and the land surface, affecting energy and water exchanges, as well as landscape properties^{10,11,18}, thereby influencing wildfire dynamics.

In this study, we provide a novel perspective by demonstrating the feedback of peak photosynthesis timing on wildfire activities, particularly in northern ecosystems. Our findings are supported by various sources of wildfire data, including detailed terrestrial fire perimeters and large-scale MODIS products, as well as observations of peak photosynthesis timing based on satellite solar-induced chlorophyll fluorescence (SIF) and the normalized difference vegetation index (NDVI). Moreover, our simulation results using an earth system model confirm the climate feedback resulting from advanced summer vegetation phenology in the middle and high latitudes of the Northern Hemisphere. These results highlight the relationships among plant growth, drought conditions and subsequent wildfire activities. A

key contribution of our study is the emphasis on the seasonal dynamics of wildfires, which have received relatively less attention in previous studies. We identify a strong influence of vegetation phenology on the seasonality of wildfires. Notably, a substantial portion (60-80%) of burned area and CO₂ emissions from wildfires occurs after the peak photosynthesis timing (Supplementary Fig. S5). Additionally, approximately 65% of the analyzed pixels exhibit maximum wildfire activity following peak photosynthesis timing (Supplementary Fig. S6).

Moreover, we investigated the ability of state-of-the-art fire-vegetation models (FireMIP models) to replicate the observed effects of peak photosynthesis timing on burned area. In agreement with the empirical results, the simulations show that an earlier PPT results in an increase in wildfire activity. FireMIP models have been shown to adequately represent the seasonal peak timing in GPP and the seasonality in burned area¹⁵, explaining why they were able to replicate the direction of the correlation between PPT and burned area. However, our findings also reveal that the FireMIP models do not capture the magnitude of this effect, meaning that they largely underestimated the sensitivity of burned area to PPT by up to 270% compared to satellite observations. This discrepancy may arise from the failure to adequately represent pre-season fuel build-up and its subsequent effect on burned area in the models^{15,19}. These limitations in capturing pre-season fuel dynamics can contribute to the divergent sensitivities observed in the models.

Using empirical and mechanistic models, we attempted to understand the connection between peak photosynthesis timing and wildfires, taking into account both biophysical and biogeochemical factors. Our findings suggest that the timing of leaf senescence plays a crucial role in connecting peak photosynthesis timing and wildfire activities. An advanced peak photosynthesis timing leads to earlier leaf senescence, independent of climate and greening effects. This finding is consistent with previous studies highlighting the influence of greener and more productive spring and summer periods on driving earlier autumn leaf senescence^{20,21}. The earlier leaf senescence likely contributes to an increased and earlier accumulation of dead fuel (Supplementary Fig. S4), which possesses lower moisture content than live fuel, making it more susceptible to weather conditions and more flammable²². As a result, it contributes to the occurrence of wildfires²³ and the expansion of burned areas²⁴.

In addition to the influence of leaf senescence on wildfire activity, our study reveals that an earlier peak photosynthesis timing also has significant impacts on atmospheric conditions and water availability, further exacerbating wildfire risks. Both observations and numerical simulations show that an earlier peak photosynthesis timing increases atmospheric vapor pressure deficit (VPD) and climatic water deficit (CWD), which create favorable conditions for fire ignition and propagation. These biophysical feedbacks are related to increased soil moisture stress resulting from extensive water use under earlier and enhanced vegetation growth and subsequent evaporative water loss^{12,13,18}. As a consequence, the progressive soil moisture deficit reduces evaporative cooling, increases sensible heat flux, amplifies temperature anomalies^{25,26}, and inhibits locally convective precipitation. These changes lead to earlier wildfire outbreaks and an increase in the area being burned. The absence of accounting for these

biophysical feedback loops between vegetation and climate likely explain why the current fire-vegetation models drastically underestimate the extent of how changes in peak photosynthesis timing can influence wildfire occurrence and the subsequent expansion of burned areas.

In summary, our findings reveal that earlier peak photosynthesis timing has significant implications for wildfire activities, leading to an acceleration of wildfire outbreaks and an expansion of burned areas. This relationship is driven by the interplay of multiple factors, including enhanced atmospheric aridity (VPD), heightened plant water stress (CWD), and the increased availability of combustible material due to earlier leaf senescence (DFS). However, current fire-vegetation models underestimate the sensitivity of burned area to peak photosynthesis timing, despite capturing the negative correlation. The seasonal variations in plant growth have the potential to alter the distribution of fuel sources, and the biophysical feedback mechanisms resulting from these changes can influence local climate conditions by modulating energy and water exchange between terrestrial ecosystems and the atmosphere¹⁸. Therefore, it is crucial to consider these processes and underlying mechanisms in both data-driven and process-based fire models. Incorporating the effects of peak photosynthesis timing on local climate and wildfire activities can improve predictions of the magnitude and seasonality of wildfire outbreaks. By considering the bioclimatic interactions among climate, vegetation and fire, we can better understand the dynamics of wildfires and improve our ability to anticipate and mitigate their impacts.

Declarations

Data availability

All data used in this study are available online. The specific links for each observation dataset and FireMIP models outputs are presented in Table S1 and Table S2.

Code availability

All data analyses and modeling were performed using Python. The codes for the phenological models are available at <https://doi.org/10.5281/zenodo.5829780>. The CESM2.2 codes can be publicly accessed from <https://www.cesm.ucar.edu/models/cesm2>. Other codes are available upon request to the corresponding authors.

ACKNOWLEDGMENTS

We are deeply indebted to the data providers and the managers of the FireMIP models output data. We also give our sincere thanks to all data providers listed in Table S1 for continuous efforts and for sharing their data. This work was funded by the National Key Research and Development Program of China (2019YFA0606601 and 2019YFA0606603). C.W. was funded by the National Natural Science Foundation of China (42125101) and the CAS Interdisciplinary Innovation Team (JCTD-2020-05). J.W. was supported by the Programme of Kezhen-Bingwei Excellent Young Scientists of the Institute of Geographic Sciences and Natural Resources Research, Chinese Academy of Sciences (2022RC006). C.M.Z. was funded by SNF

Ambizione grant PZ00P3_193646. J.P. was funded by the TED2021-132627B-I00 grant funded by the Spanish MCIN, AEI/10.13039/501100011033, the European Union NextGenerationEU/PRTR, the Fundación Ramón Areces project CIVP20A6621.

Contributions

C.W. designed the research. G.L., C.W., Y.Z. and J.W. wrote the first draft of the manuscript. G.L. and J.L. performed the observation and fire models analyses and visualization. J.W. conducted the numerical simulations and analyzed the model outputs. All authors assessed the research analyses and contributed to the writing of the manuscript.

Competing interests

The authors declare no competing financial interests.

References

1. Bowman, D. M. J. S. *et al.* Vegetation fires in the Anthropocene. *Nature Reviews Earth & Environment* **1**, 500-515 (2020).
2. Descals, A. *et al.* Unprecedented fire activity above the Arctic Circle linked to rising temperatures. *Science* **378**, 532-537 (2022).
3. Zheng, B. *et al.* Record-high CO₂ emissions from boreal fires in 2021. *Science* **379**, 912-917 (2023).
4. Pellegrini, A. F. A. *et al.* Fire effects on the persistence of soil organic matter and long-term carbon storage. *Nature Geoscience* **15**, 5-13 (2021).
5. Wilkinson, S. L. *et al.* Wildfire and degradation accelerate northern peatland carbon release. *Nature Climate Change* **13**, 456-461 (2023).
6. Grünig, M., Seidl, R. & Senf, C. Increasing aridity causes larger and more severe forest fires across Europe. *Global Change Biology* **29**, 1648-1659 (2023).
7. Jain, P., Castellanos-Acuna, D., Coogan, S. C. P., Abatzoglou, J. T. & Flannigan, M. D. Observed increases in extreme fire weather driven by atmospheric humidity and temperature. *Nature Climate Change* **12**, 63-70 (2022).
8. Jones, M. W. *et al.* Global and Regional Trends and Drivers of Fire Under Climate Change. *Reviews of Geophysics* **60**, e2020RG000726 (2022).
9. Myers-Smith, I. H. *et al.* Complexity revealed in the greening of the Arctic. *Nature Climate Change* **10**, 106-117 (2020).
10. Piao, S. *et al.* Characteristics, drivers and feedbacks of global greening. *Nature Reviews Earth & Environment* **1**, 14-27 (2020).
11. Peñuelas, J., Rutishauser, T. & Filella, I. Phenology Feedbacks on Climate Change. *Science* **324**, 887-888 (2009).

12. Lian, X. *et al.* Summer soil drying exacerbated by earlier spring greening of northern vegetation. *Sci Adv* **6**, eaax0255 (2020).
13. Bastos, A. *et al.* Direct and seasonal legacy effects of the 2018 heat wave and drought on European ecosystem productivity. *Science Advances* **6**, eaba2724 (2020).
14. Xu, X., Riley, W. J., Koven, C. D., Jia, G. & Zhang, X. Earlier leaf-out warms air in the north. *Nature Climate Change* **10**, 370-375 (2020).
15. Hantson, S. *et al.* Quantitative assessment of fire and vegetation properties in simulations with fire-enabled vegetation models from the Fire Model Intercomparison Project. *Geoscientific Model Development* **13**, 3299-3318 (2020).
16. Andela, N. *et al.* A human-driven decline in global burned area. *Science* **356**, 1356-1362 (2017).
17. Pausas, J. G. & Keeley, J. E. Wildfires and global change. *Frontiers in Ecology and the Environment* **19**, 387-395 (2021).
18. Piao, S. *et al.* Plant phenology and global climate change: Current progresses and challenges. *Glob Chang Biol* **25**, 1922-1940 (2019).
19. Forkel, M. *et al.* Emergent relationships with respect to burned area in global satellite observations and fire-enabled vegetation models. *Biogeosciences* **16**, 57-76 (2019).
20. Zani, D., Crowther, T. W., Mo, L., Renner, S. S. & Zohner, C. M. Increased growing-season productivity drives earlier autumn leaf senescence in temperate trees. *Science* **370**, 1066-1071 (2020).
21. Zohner, C. M. *et al.* Effect of climate warming on the timing of autumn leaf senescence reverses after the summer solstice. *Science* **381**, eadf5098 (2023).
22. Matthews, S. Dead fuel moisture research: 1991–2012. *International Journal of Wildland Fire* **23** (2014).
23. Nolan, R. H., Boer, M. M., Resco de Dios, V., Caccamo, G. & Bradstock, R. A. Large-Scale, Dynamic Transformations in Fuel Moisture Drive Wildfire Activity across Southeastern Australia. *Geophysical Research Letters* **43**, 4229-4238 (2016).
24. Nolan, R. H. *et al.* Causes and consequences of eastern Australia's 2019-20 season of mega-fires. *Glob Chang Biol* **26**, 1039-1041 (2020).
25. Seneviratne, S. I. *et al.* Investigating soil moisture–climate interactions in a changing climate: A review. *Earth-Science Reviews* **99**, 125-161 (2010).
26. Stéfanon, M., Drobinski, P., D'Andrea, F. & de Noblet-Ducoudré, N. Effects of interactive vegetation phenology on the 2003 summer heat waves. *Journal of Geophysical Research: Atmospheres* **117** (2012).

Methods

Satellite-based peak vegetation growth

We employed two metrics to monitor the peak vegetation growth in northern ecosystems ($>30^{\circ}\text{N}$) during the period of 2001-2018. These metrics included the maximum solar-induced chlorophyll fluorescence (SIF) and the corresponding peak photosynthesis timing (SIF_{max} and PPT_{SIF}). SIF serves as a direct indicator of photosynthetic activity²⁷⁻²⁹, and we utilized a monthly temporally corrected long-term satellite SIF product (LT_SIFc) with a resolution of 0.05° to track the seasonal variations in SIF³⁰. Additionally, we utilized the normalized difference vegetation index (NDVI) and its peak photosynthesis timing (PPT_{NDVI}). NDVI is a widely-used ecological index that reflects vegetation photosynthesis and phenology^{10,18}. The long-term dynamics of NDVI were derived from the MODIS vegetation indices product (MOD13C1 V6), which provides 16-day 0.05° NDVI observations, enabling the tracking of vegetation seasonal dynamics. To obtain yearly peak vegetation growth values (i.e., PPT_{SIF} , SIF_{max} , PPT_{NDVI} , and NDVI_{max}), we employed the SG-cubic spline method, following the approach proposed by ref.³¹ (Supplementary Fig. S2). Furthermore, we utilized a 8-day spatiotemporally continuous GOSIF product with a resolution of 0.05° to extract the maximum photosynthesis and its timing³², and consistent results were obtained (Supplementary Fig. S7-S9). The maximum values and PPT were upscaled to a resolution of 0.25° using bilinear and nearest interpolations, respectively. To mitigate the influence of abnormally high values in SIF_{max} and NDVI_{max} , we employed the 95th quantile to remove outliers.

Terrestrial fire perimeters

We utilized terrestrial fire perimeter (FP) products from Canada (National Burned Area Composite, NBAC), USA (Monitoring Trends in Burn Severity, MTBS), and Europe (European Forest Fire Information System, EFFIS) to extract information on wildfire timing (FT) and burned area (BA) following the PPT for the period of 2001-2018 (Supplementary Fig. S1). In the case of the USA, the analyses using FP products excluded Alaska and Hawaii. For Europe, we selected three countries, namely Portugal, Spain, and Italy, which had the largest annual averaged burned areas based on the EFFIS statistics (<https://effis.jrc.ec.europa.eu/apps/effis.statistics/estimates>). These FP products, with a finer resolution compared to global remote sensing products, were compiled through ground-based and airborne surveys and/or fine-scale satellite imagery (e.g., 30 m Landsat imagery)^{33,34}. They provided precise date information for each fire polygon. To align with the MODIS burned area product, the FP data were initially rasterized at a spatial resolution of 0.00025° (approximately 30 m), ensuring good correspondence between fire pixels and fire perimeters. Subsequently, FT and BA were calculated within each 0.25° grid cell, which covered an area of 1000×1000 30 m pixels. For each grid cell, FT represented the date of the first wildfire outbreak DOY following the peak photosynthesis timing, while BA represented the total burned area after PPT. The detailed processing steps for the FP product are presented in Supplementary Fig. S10.

Satellite wildfire product

We also utilized the MODIS burned area product (MCD64A1 V6) with a 500 m resolution to examine the correlation between PPT and wildfire activities across the entire northern ecosystems ($>30^{\circ}\text{N}$) from 2001 to 2018³⁵. Using the “burn of date” information and considering uncertainty, we calculated FT and BA after PPT within each 0.25° grid cell (covering an area of 60×60 500 m pixels). We excluded burned pixels with high uncertainty ($>50\%$) and those located in croplands and non-vegetated areas. The plant functional types (PFTs) and non-vegetated areas were identified using the IGBP classification scheme provided in the MODIS land cover type product (MCD12Q1 V6) for the period of 2001-2018. Note that the pixels repeatedly marked as burned in one year were only recorded once in burned area calculation.

VPD, CWD, and DFS

To elucidate the linkages between PPT and wildfire activities, we considered three factors: VPD, representing atmospheric aridity and fire weather⁷; CWD, indicating plant water stress²; and DFS, reflecting leaf supply due to leaf senescence³⁶. Monthly VPD was calculated based on air temperature (T) and dewpoint temperature (T_d) at 2 m above the surface³⁷, derived from ERA5-Land monthly averaged products with a 0.1° resolution³⁸. Monthly CWD, representing the difference between potential and actual evapotranspiration, was obtained from the TerraClimate dataset with a $1/24^{\circ}$ resolution³⁹. DFS based on SIF was derived from the vegetation photosynthetic phenology dataset with a 0.05° resolution⁴⁰. This dataset was retrieved by the method of combining smoothing splines with multiple change-point detection, in which we selected the end of the growing season determined by the amplitude threshold of 50%⁴⁰. The DFS based on NDVI was extracted from the half-monthly MODIS NDVI product (MOD13C1 V6) with a 0.05° resolution, following the method proposed by ref. ⁴¹. These factors were upscaled to a 0.25° resolution using bilinear interpolation, except for DFS using nearest method. We used the monthly difference of SIF/NDVI from July to October (representing the entire senescence period in northern ecosystems³⁶) to represent the accumulated dead fuel due to leaf senescence ($\Delta\text{SIF}/\Delta\text{NDVI}$). Then, spearman correlation between DFS and $\Delta\text{SIF}/\Delta\text{NDVI}$ was conducted (Supplementary Fig. S4).

Other climatic data

To characterize the climatic conditions in the northern ecosystems for the period of 2001-2018, we utilized the ERA5-Land monthly averaged products with a 0.1° resolution, provided by the European Centre for Medium-Range Weather Forecasts (ECMWF)³⁸. The climatic variables considered included air temperature (T), total precipitation (PRE), and volumetric soil water content at the 0-7 cm layer (SM). These climatic variables were resampled to a 0.25° resolution using bilinear interpolation.

Analyses

Partial correlation analysis was employed to investigate the impact of PPT on FT and BA. Two partial correlation scenarios were designed: (1) PPT versus FT and BA, while removing the effects of T, PRE, and the maximum photosynthesis; (2) the maximum photosynthesis versus FT and BA, while eliminating the effects of T, PRE, and PPT. It is important to note that the climatic conditions were represented by the monthly averaged T and accumulated PRE from the month of PPT to FT, reflecting the preseason forcing that controls wildfire outbreak. For BA, the climatic conditions (T and PRE) were calculated from the month of PPT to November, representing the climate during the potential fire season that influences wildfire propagation and total burned areas.

VPD, CWD, and DFS were utilized as explanatory factors between peak photosynthesis timing and wildfire activities. Partial correlation analysis was employed to elucidate the effect of PPT on these explanatory factors, and subsequently, the impact of these factors on FT and BA after accounting for the effects of T, PRE, SM, and the maximum photosynthesis. VPD, CWD, T, and SM were averaged from the month of PPT to FT, while PRE was accumulated.

To quantitatively explore the underlying mechanisms between PPT and wildfire activities, path analysis was employed. Three pathways were considered: PPT-VPD-wildfire, PPT-CWD-wildfire, and PPT-DFS-wildfire (Supplementary Fig. S3). The path analysis was conducted on a pixel-by-pixel basis. Five metrics were selected to assess the goodness of fit of the model, including the Goodness-of-fit Index ($GFI \geq 0.95$), Comparative Fit Index ($CFI \geq 0.90$), Root Mean Square Error of Approximation ($RMSEA < 0.1$), Non-Normed Fit Index ($NNFI \geq 0.92$), and Standardized Root Mean Square Residual ($SRMR < 0.08$). A model for each pixel was deemed reliable when three out of the five criteria were met⁴². The regional standard path coefficient was calculated as the regional mean, considering the goodness of fit of the model and the significance level of the path coefficient ($p\text{-value} < 0.1$). The corresponding standard deviation was considered as the uncertainty. The goodness of fit of the models and the standard path coefficient of each path for different sources of photosynthesis and wildfire observations are presented in Supplementary Fig. S11-S14.

To enhance the reliability and spatial consistency of the estimates by increasing the sample size, a 9×9 spatial moving window ($2.25^\circ \times 2.25^\circ$) was employed to represent the central grid cell during partial correlation and path analysis. The partial correlation analyses were based on the anomaly of each factor, obtained by subtracting the multi-year mean from the original data. To ensure model stability in the path analysis, normalized anomalies of each factor were used to fit the model. All analyses were conducted solely on burned grid cells.

Model configuration and experimental design

We used the Community Earth System Model version 2.2, which is the latest version of the coupled Earth system model developed at the National Center for Atmospheric Research in collaboration with universities and other research institutions⁴³. We ran the model for AMIP-type simulations with two-way

coupled atmosphere (Community Atmosphere Model version 6, CAM6) and land (Community Land Model version 5, CLM5) components, and prescribed sea surface temperature and sea ice concentration of present-day climatology (1995-2005), with biogeochemistry model being inactive. The CAM6 and CLM5 use a nominal 2° (1.9° in latitude and 2.5° in longitude) horizontal resolution with 32 vertical levels and a model top pressure at 3.64 hPa. Satellite-observed vegetation phenology, monthly leaf area index (LAI), stem area index (SAI) and other vegetation features around the year 2000 are prescribed for each plant functional types (PFT) in CLM5. Monthly PFT LAI values were produced based on the 1-km MODIS-derived monthly grid cell average LAI^{44,45}. The SAI was calculated from the monthly PFT LAI using the method proposed by ref. ⁴⁶.

To spin-up the earth system model, we first ran it for 50 simulation years starting from prescribed initial conditions. Then we employed a consistent set of final restart files for the initial conditions in following 100-year control and sensitivity simulations. We kept all the vegetation parameters unchanged in the control simulation, but modified the prescribed LAI and SAI of temperate and boreal trees in the Northern Hemisphere (>30°N) in the sensitivity simulation by shifting their summertime (June, July and August) growing phases earlier by 10 days. Specifically, we obtained summer daily LAI and SAI series by linearly interpolating between monthly values and replaced the original indices with those 10 days later. Note that the values of LAI and SAI in other seasons remained unchanged. Considering that the annual maximum photosynthesis for most northern boreal and temperate trees occurs in summer (Supplementary Fig. S6), the simulated differences between the control and sensitivity experiments largely represent the climatic feedbacks from an advanced PPT in the Northern Hemisphere.

FireMIP

To investigate whether the state-of-the-art fire-vegetation models were able to reproduce the observed impacts of PPT on wildfire activities, we employed the outputs of FireMIP models to compare with satellite results over the period of 2001-2012⁴⁷. The FireMIP aims to evaluate the advanced global fire models and promote projections of global fire characteristics and impacts on ecosystems and human societies under the ongoing climate change¹⁵. These models, with varied complexity including empirical and process-based models, and different representations of the impacts of climate conditions, vegetation productivity, and human activities on fire occurrence, have divergent abilities to reproduce the spatiotemporal patterns of global wildfires^{15,16}. We utilized the seven out of nine FireMIP models (including CLM, JSBACH-SPITFIRE, LPJ-GUESS-SPITFIRE, ORCHIDEE-SPITFIRE, CTEM, JULES-INFERN0, and LPJ-GUESS-SIMFIRE-BLAZE) that can model the monthly GPP and BA with divergent spatial resolutions (Table S2), which allows us to calculate PPT based on the SG-cubic spline method³¹ and subsequent BA.

We examined the abilities of these models compared with satellite SIF derived from LT_SIFc in two aspects: (1) using partial correlation to qualitatively compare the correlation between PPT and subsequent burned area; (2) utilizing ridge regression to quantificationally estimate the sensitivity of

burned area to PPT after eliminating the effects of T, PRE, and the maximum photosynthesis. To mitigate the implication of divergent spatial resolutions among seven FireMIP models and satellite SIF product, we calculated the area-weighted mean and 95% confidence interval of sensitivities for the entire northern ecosystems.

References

- 27 Joiner, J. *et al.* First observations of global and seasonal terrestrial chlorophyll fluorescence from space. *Biogeosciences* **8**, 637-651 (2011).
- 28 Frankenberg, C. *et al.* New global observations of the terrestrial carbon cycle from GOSAT: Patterns of plant fluorescence with gross primary productivity. *Geophysical Research Letters* **38** (2011).
- 29 Guanter, L. *et al.* Global and time-resolved monitoring of crop photosynthesis with chlorophyll fluorescence. *Proceedings of the National Academy of Sciences* **111**, E1327-E1333 (2014).
- 30 Wang, S. *et al.* Temporally corrected long-term satellite solar-induced fluorescence leads to improved estimation of global trends in vegetation photosynthesis during 1995–2018. *ISPRS Journal of Photogrammetry and Remote Sensing* **194**, 222-234 (2022).
- 31 Wang, X. & Wu, C. Estimating the peak of growing season (POS) of China's terrestrial ecosystems. *Agricultural and Forest Meteorology* **278** (2019).
- 32 Li, X. & Xiao, J. A Global, 0.05-Degree Product of Solar-Induced Chlorophyll Fluorescence Derived from OCO-2, MODIS, and Reanalysis Data. *Remote Sensing* **11** (2019).
- 33 Hall, R. J. *et al.* Generating annual estimates of forest fire disturbance in Canada: the National Burned Area Composite. *International Journal of Wildland Fire* **29** (2020).
- 34 Picotte, J. J. *et al.* Changes to the Monitoring Trends in Burn Severity program mapping production procedures and data products. *Fire Ecology* **16** (2020).
- 35 Giglio, L., Boschetti, L., Roy, D. P., Humber, M. L. & Justice, C. O. The Collection 6 MODIS burned area mapping algorithm and product. *Remote Sens Environ* **217**, 72-85 (2018).
- 36 Zhang, Y. *et al.* Autumn canopy senescence has slowed down with global warming since the 1980s in the Northern Hemisphere. *Communications Earth & Environment* **4** (2023).
- 37 Yuan, W. *et al.* Increased atmospheric vapor pressure deficit reduces global vegetation growth. *Science Advances* **5**, eaax1396 (2019).
- 38 Muñoz-Sabater, J. *et al.* ERA5-Land: a state-of-the-art global reanalysis dataset for land applications. *Earth System Science Data* **13**, 4349-4383 (2021).

- 39 Abatzoglou, J. T., Dobrowski, S. Z., Parks, S. A. & Hegewisch, K. C. TerraClimate, a high-resolution global dataset of monthly climate and climatic water balance from 1958-2015. *Sci Data* **5**, 170191 (2018).
- 40 Fang, J. *et al.* Vegetation photosynthetic phenology dataset in northern terrestrial ecosystems. *Sci Data* **10**, 300 (2023).
- 41 Shen, M. *et al.* Greater temperature sensitivity of vegetation greenup onset date in areas with weaker temperature seasonality across the Northern Hemisphere. *Agricultural and Forest Meteorology* **313** (2022).
- 42 Gao, S. *et al.* An earlier start of the thermal growing season enhances tree growth in cold humid areas but not in dry areas. *Nat Ecol Evol* **6**, 397-404 (2022).
- 43 Danabasoglu, G. *et al.* The Community Earth System Model Version 2 (CESM2). *Journal of Advances in Modeling Earth Systems* **12** (2020).
- 44 Lawrence, P. J. & Chase, T. N. Representing a new MODIS consistent land surface in the Community Land Model (CLM 3.0). *Journal of Geophysical Research* **112** (2007).
- 45 Myneni, R. B. *et al.* Global products of vegetation leaf area and fraction absorbed PAR from year one of MODIS data. *Remote sensing of environment* **83**, 214-231 (2002).
- 46 Zeng, X., Shaikh, M., Dai, Y., Dickinson, R. E. & Myneni, R. Coupling of the Common Land Model to the NCAR Community Climate Model. *Journal of Climate* **15**, 1832-1854 (2002).
- 47 Hantson, S. *et al.* Model outputs: Quantitative assessment of fire and vegetation properties in historical simulations with fire-enabled vegetation models from the Fire Model Intercomparison Project [Data set]. *Zenodo* <https://doi.org/10.5281/zenodo.3555562> (2019).

Figures

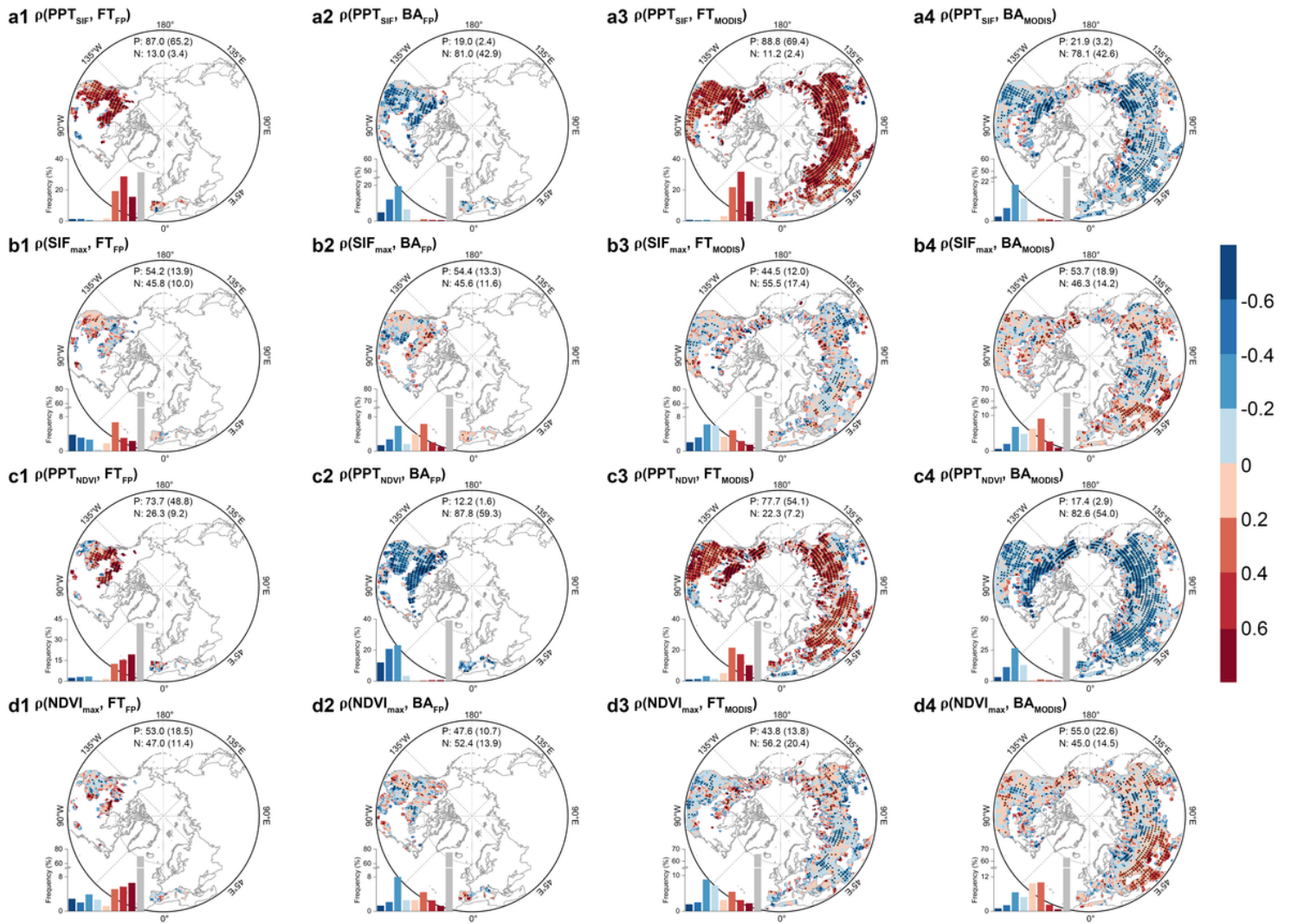


Figure 1

Controls of peak vegetation growth on wildfire outbreak and burned area in northern ecosystems (>30°N). Partial correlations (ρ) between peak vegetation photosynthesis (maximum photosynthesis and its timing [PPT]) and wildfire timing (FT) and burned area (BA) for different sources of photosynthesis and wildfire observations. **a-d**, SIF-derived timing (PPT_{SIF}) and maximum (SIF_{max}), and NDVI-derived timing (PPT_{NDVI}) and maximum (NDVI_{max}), respectively. **1-4** indicate the FT and BA derived from terrestrial fire perimeters (FT_{FP} and BA_{FP}) and MODIS observations (FT_{MODIS} and BA_{MODIS}), respectively. Black dots indicate the regions with significant partial correlations (p -value<0.1). P and N indicate the percentage of positive and negative correlations, respectively. PPT positively correlated with wildfire timing but had a negative effect on the burned area.

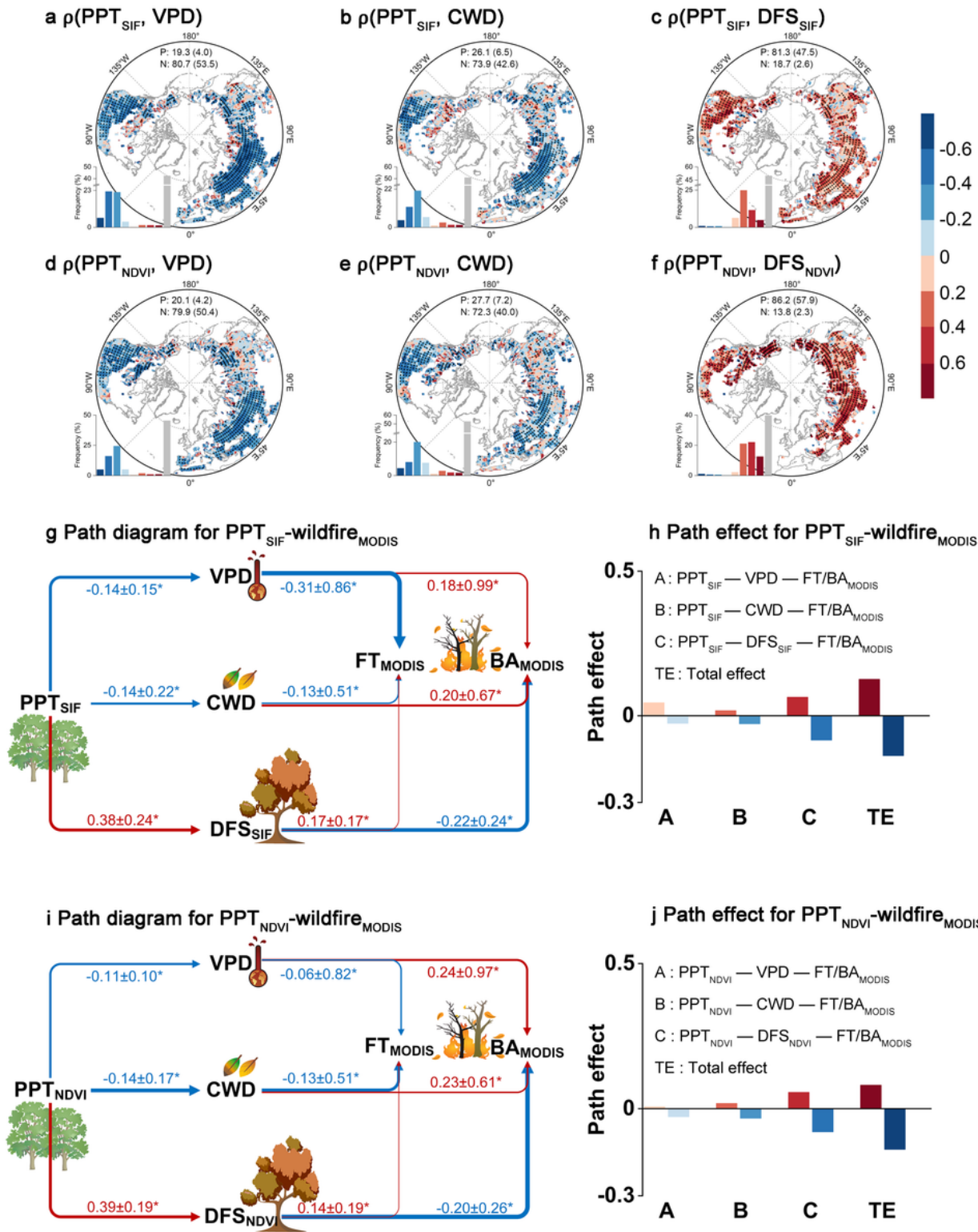


Figure 2

Potential mechanisms underlying the linkage between wildfire activity and peak photosynthesis timing. **a-f**, Spatial patterns of partial correlations: PPT_{SIF} versus VPD (**a**), PPT_{SIF} versus CWD (**b**), PPT_{SIF} versus DFS_{SIF} (**c**), PPT_{NDVI} versus VPD (**d**), PPT_{NDVI} versus CWD (**e**), and PPT_{NDVI} versus DFS_{NDVI} (**f**). Black dots indicate the regions with significant partial correlations ($p\text{-value} < 0.1$). **g-j**, Path diagrams and path effects for $\text{PPT}_{\text{SIF}}\text{-wildfire}_{\text{MODIS}}$ (**g-h**) and $\text{PPT}_{\text{NDVI}}\text{-wildfire}_{\text{MODIS}}$ (**i-j**). The numbers in the path diagrams represent

the mean and standard deviation of standardized path coefficients across the northern ecosystems ($>30^{\circ}\text{N}$), asterisks indicate the path coefficients are significant ($p\text{-value}<0.1$) and the colors (red and blue arrows represent positive and negative effects, respectively) and widths of the arrows represent the signs and magnitudes of the path coefficients, respectively. Red and blue bars represent path effects for PPT-FT and PPT-BA, respectively.

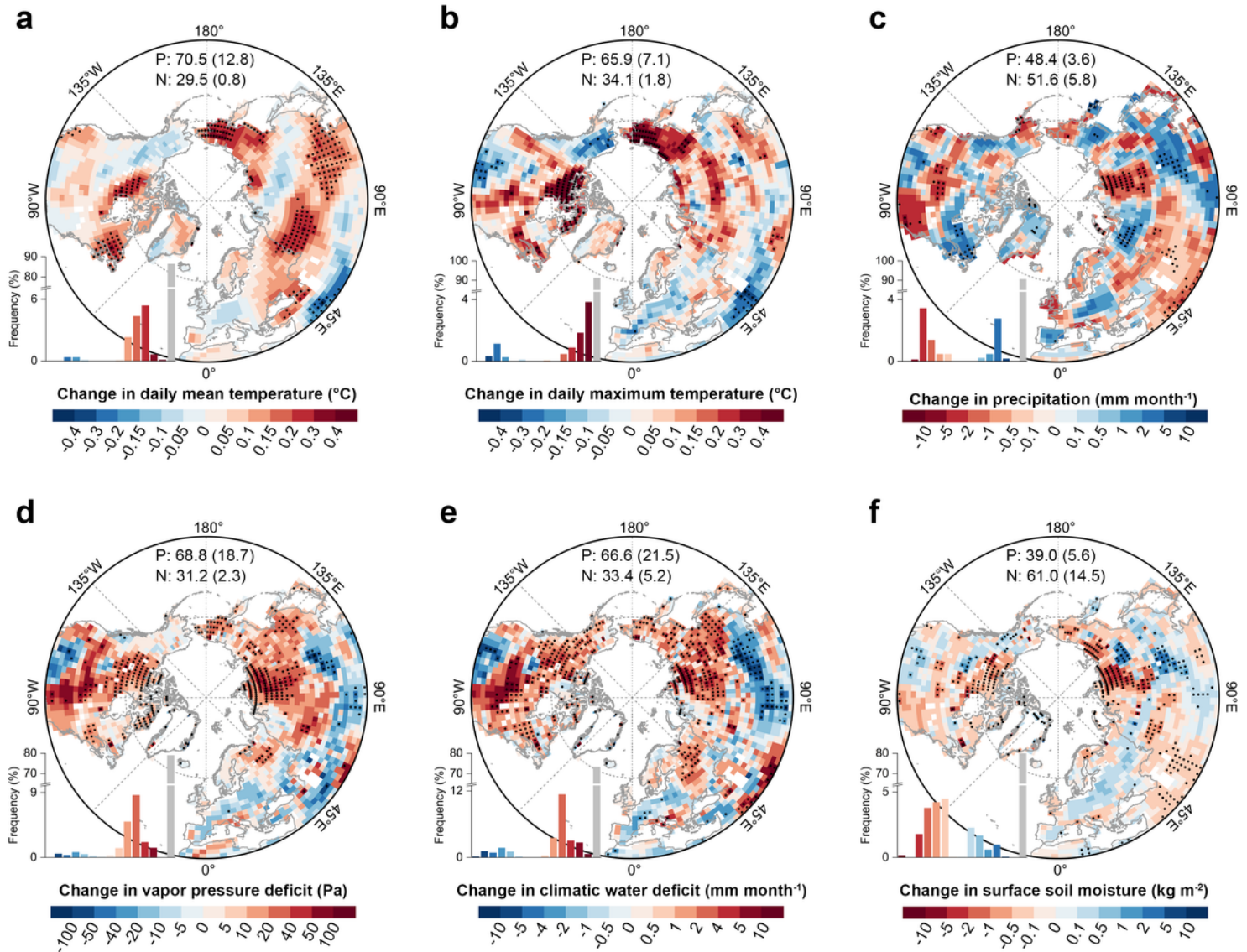


Figure 3

Earth system simulations of the effects of advanced summer phenology in northern temperate and boreal vegetation on climate parameters. Changes in daily mean and daily maximum surface air temperature (**a-b**), precipitation (**c**), vapor pressure deficit (**d**), climatic water deficit (**e**), and surface soil moisture content at a depth of 0-10 cm (**f**) in summer and autumn. The black dot marks the region with a statistically significant change (Student's t -test, $p\text{-value}<0.1$). P and N indicate the percentage of increased and decreased effects due to advanced summer phenology, respectively.

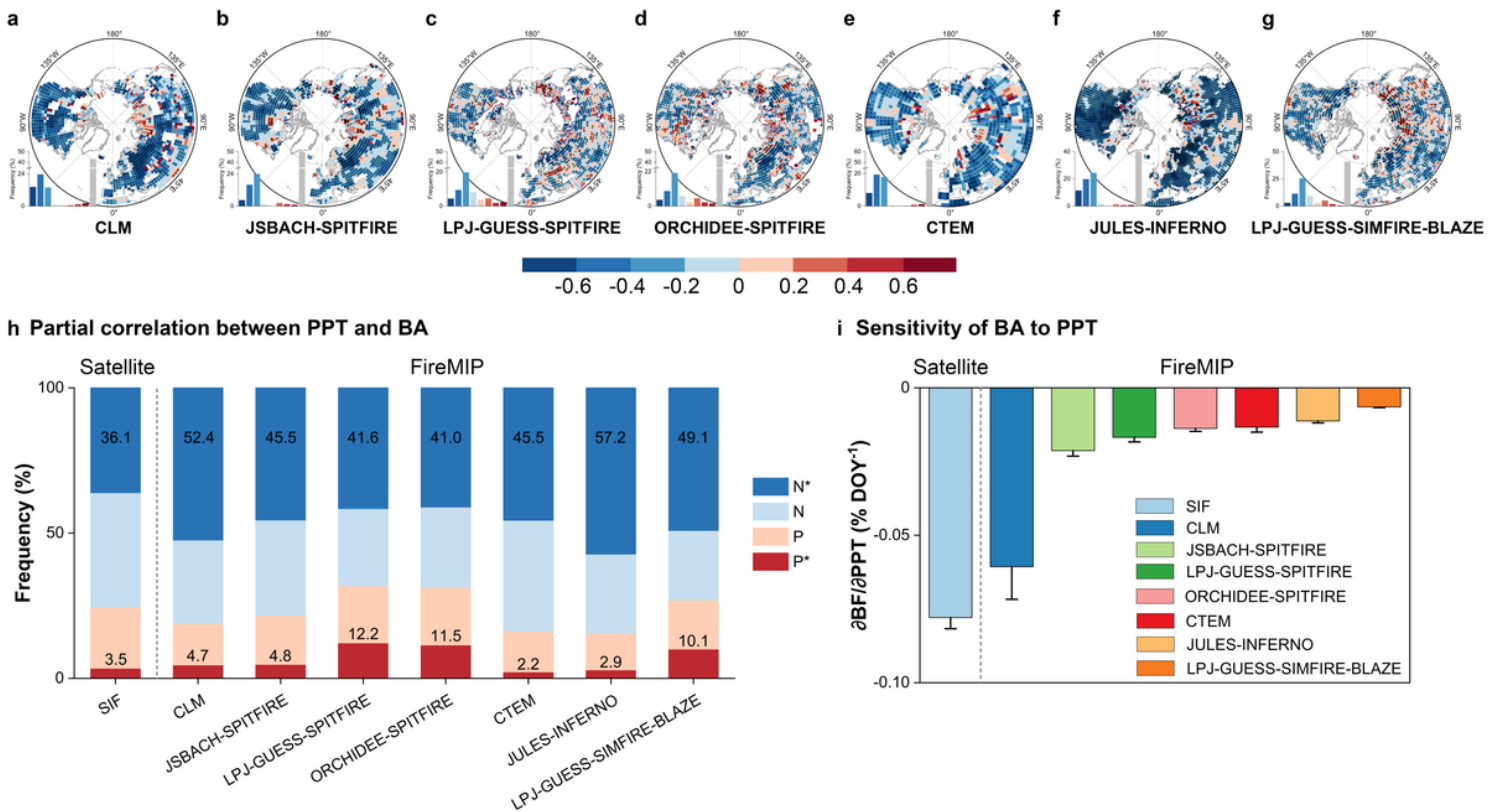


Figure 4

Comparisons of the effects of peak photosynthesis timing on burned area from satellite observations and FireMIP fire-vegetation models. Partial correlations (ρ) between PPT and BA for seven FireMIP models, including CLM (a), JSBACH-SPITFIRE (b), LPJ-GUESS-SPITFIRE (c), ORCHIDEE-SPITFIRE (d), CTEM (e), JULES-INFERN0 (f), and LPJ-GUESS-SIMFIRE-BLAZE (g). PPT and BA was derived from monthly GPP and burned area simulated by FireMIP, respectively. Comparisons of the impacts of PPT on BA between satellite observations and FireMIP models in terms of correlation (h) and sensitivity (i). The labels in h indicate the percentages of significantly negative and positive correlations (p -value <0.1). The bars and error bars in i indicate the area-weighted mean and 95% confidence interval of sensitivity, respectively. Burned area in the sensitivity analysis was represented by burned fraction (BF, %).

Supplementary Files

This is a list of supplementary files associated with this preprint. Click to download.

- [SupplementaryInformation.pdf](#)
- [ExtendedDataFigure1.png](#)
- [ExtendedDataFigure2.png](#)
- [ExtendedDataFigure3.png](#)
- [ExtendedDataFigure4.png](#)
- [ExtendedDataFigure5.png](#)

- [ExtendedDataFigure6.png](#)